Analyses of heat and water transport interactions in a proton exchange membrane fuel cell

E. Afshari, S.A. Jazayeri *

Department of Mechanical Engineering, K.N. Toosi University of Technology, Tehran, Iran

ARTICLE INFO

ABSTRACT

A two-phase non-isothermal model is developed to explore the interaction between heat and water transport phenomena in a PEM fuel cell. The numerical model is a two-dimensional simulation of the two-phase flow using multiphase mixture formulation in a single-domain approach. For this purpose, a comparison between non-isothermal and isothermal fuel cell models for inlet oxidant streams at different humidity levels is made. Numerical results reveal that the temperature distribution would affect the water transport through liquid saturation amount generated and its location, where at the voltage of 0.55 V, the maximum temperature difference is 3.7 °C. At low relative humidity of cathode, the average liquid saturation is higher and the liquid free space is smaller for the isothermal compared with the non-isothermal model. When the inlet cathode is fully humidified, the phase change will appear at the full face of cathode GDL layer, whereas the maximum liquid saturation is higher for the isothermal model. Also, heat release due to condensation of water vapor and vapor-phase diffusion which provide a mechanism for heat removal from the cell, affect the temperature distribution. Instead in the two-phase zone, water transport via vapor-phase diffusion due to the temperature gradient. The results are in good agreement with the previous theoretical works done, and validated by the available experimental data.

1. Introduction

Water management is extremely important for balancing the operation of PEM fuel cells, to avoid flooding while maintaining proper membrane hydration to achieve the best possible performance. The membrane in PEM fuel cell must be fully hydrated to get the optimal proton conductivity. However, due to low operating temperatures (70–90 °C), PEM fuel cells are prone to gas–liquid formation, particularly when they are highly humidified or at low gas flow rate conditions [1,2].

When GDL and catalyst layer become saturated with water vapor, the produced water vapor starts to condense and therefore blocks the open pores, reducing the oxygen transport to catalyst layer. Flooding becomes a major factor limiting the PEM fuel cell performance. Thermal management is also required to remove the excessive heat produced due to various heat generation, including the irreversible heat from electrochemical reactions, entropic heat, Joule heating arising from the electrolyte ionic resistance and the heat from condensation that could dry out the membrane. These heat sources, especially the irreversible reaction heat and entropic heat could rise the fuel cell temperature during operation and insuf-

ficient cooling may result in local hot spots which could reduce hydration, therefore hampering membrane performance [3]. Also having a uniform temperature distribution in the porous electrode and small temperature variation is favored where proton conductivity of the polymer electrolyte membrane strongly depends on the degree of its hydration which is affected by temperature. In this respect, a numerical model is a useful tool for understanding water and thermal management and interaction between them that is essential for proper PEM fuel cell operation.

A number of different computational approaches for PEM fuel cells have been carried out in recent years [1,3–23], considering two-phase or single-phase water transport with or without heat transfer at proton exchange membrane regions. Several studies [4–7] have attempted to predict the temperature distribution for single-phase condition. Ju et al. [8] reviewed the single-phase, non-isothermal models of PEM fuel cells in detail. Two-phase transport in PEM fuel cells has also been studied by several researchers [1,9–12]; however, the focus of these studies was primarily on the isothermal investigation of the transport phenomena. The two-phase non-isothermal model, gives a proper simultaneous description of water and thermal management with phase change. Rowe and Li [13] and Mishra et al. [14] performed a study on water and thermal management in PEM fuel cell considering a steady-state, one-dimensional approach. Berning and Djlali [15] presented a model based on the unsaturated flow theory with

---
* Corresponding author. Tel.: +98 21 88674841; fax: +98 21 88674844.
E-mail address: Jazayeri@kntu.ac.ir (S.A. Jazayeri).

Nomenclature

a	water activity or specific electrochemically active area ($m^2\,m^{-3}$)
A	superficial electrode area (m^2)
C^i	molar concentration of species i ($mol\,m^{-3}$)
c_p	specific heat capacity ($J\,kg^{-1}\,K^{-1}$)
D^i	mass diffusivity of species i ($m^2\,s^{-1}$)
EW	equivalent weight of dry membrane ($kg\,mol^{-1}$)
F	Faraday constant, 96,487 ($C\,mol^{-1}$)
h_{fg}	latent heat of evaporation of water ($kJ\,kg^{-1}$)
i_0	exchange current density ($A\,m^{-2}$)
I	current density ($A\,m^{-2}$)
j	transfer current ($A\,m^{-3}$)
J	Leverett function
j_l	mass flux of liquid phase ($kg\,m^{-2}\,s^{-1}$)
k	thermal conductivity ($W\,m^{-1}\,K^{-1}$)
k_{rk}	relative permeability of phase k
K	hydraulic permeability (m^2)
M^i	molecular weight of species i ($kg\,mol^{-1}$)
mf_k^i	mass fraction of species i in phase k
$\dot{m}_{fg}$	mass flow rate ($kg\,s^{-1}$)
n	the direction normal to the surface
n_d	electro-osmotic drag coefficient
P	pressure (Pa)
R	universal gas constant, 8.314 $J\,mol^{-1}\,K^{-1}$
RH	relative humidity
s	liquid saturation
S	source term
T	temperature (K)
$\bar{u}$	velocity vector ($m\,s^{-1}$)
U_0	thermodynamic equilibrium potential (V)
V_{cell}	cell potential (V)
V	volume (m^3)
x	mole fraction

Greek symbols

α	transfer coefficient for reaction
ε	volume fraction
ε_{mc}	volume fraction of ionomer phase in catalyst layer
ϕ	potential (V)
γ_c	advection coefficient for transport of species
γ_h	advection coefficient for heat transfer
η	overpotential (V)
κ	ionic conductivity ($S\,m^{-1}$)
λ	polymer water content
λ_k	relative mobility of phase k
μ	viscosity (Pa s)
ν	kinematic viscosity ($m^2\,s^{-1}$)
θ_c	contact angle (°)
ρ	density ($kg\,m^{-3}$)
$\rho_{dry,m}$	dry membrane density ($kg\,m^{-3}$)
σ	surface tension ($N\,m^{-1}$)
ζ	stoichiometry flow ratio

Subscripts

a	anode
c	cathode or capillary
e	electrolyte
in	inlet
g	gas
l	liquid
ref	reference
sat	saturation
s	solid
0	standard condition, 298.15 K and 101.3 kPa

Superscripts

eff	effective
H_2	hydrogen
H_2O	water
O_2	oxygen

the assumption of constant gas pressure across the porous media. In this model two separate computational domains had to be set up, one for gas flow channels and the other for GDL to accommodate the heat transfer through the solid matrix of the porous media. Mazumder and Cole [16] adopted the M^2 model to investigate the formation and transport of liquid water in PEM fuel cells for a three-dimensional geometry. In this model the cell was assumed to be isothermal by setting the thermal conductivity in all regions to be very high, therefore neglecting the thermal effects on phase change. Birgersson et al. [17] presented a two-dimensional model based on the multifluid approach, which is in contrast to the M^2 model. Wang and Wang [18] developed a non-isothermal, two-phase model based on the M^2 approach and identified the importance of water transport as well as heat removal via vapor-phase diffusion with variable temperature. The model presented by Hwang [19] illustrates the behaviors of the two-phase flow and heat transfer in a porous electrode. Pasaogullari et al. [20] developed a model to investigate heat and mass transfer in the GDL cathode simultaneously. Also Yuan and Sunden [21] presented a non-isothermal, two-phase model in multi-dimensional situations. However, only the cathode GDL and gas channel were considered. Afshari and Jazayeri [22,23] developed a mathematical model for the heat transfer and liquid water formation in a PEM fuel cell and investigated the thermal and water management effects on cell performance.

In the present study, a two-dimensional, two-phase, non-isothermal, and single-domain model together with coupled electrochemical relations is analyzed and the effects of interactions between water and heat transfer with phase changes in a PEM fuel cell are investigated.

2. Mathematical modeling

The model domain consists of the following subregions: the gas channels, gas diffusion layers (GDLs), catalyst layers for both the anode and cathode sides, with the membrane in the middle. Fuel and oxidant flow through channels and are distributed into anode and cathode. Hydrogen oxidation and oxygen reduction reactions occur only within the active catalyst layers. The fuel and oxidant flow rates can be described by a stoichiometric flow ratio, ζ, defined as the amount of reactant in the gas chamber fed to the amount required by the electrochemical reaction [18]. That is

$$\varsigma_a = C_{H_2,in} U_{a,in} \frac{2F}{I_{ref}} \frac{A_{a,in}}{A} \qquad (1)$$

$$\varsigma_c = C_{O_2,in} U_{c,in} \frac{4F}{I_{ref}} \frac{A_{c,in}}{A} \qquad (2)$$

where A is the superficial electrode area, and A_a, A_c, $U_{in,a}$ and $U_{in,c}$ are the flow cross-sectional areas and the inlet velocities of the anode and cathode gas channels, respectively. The stoichiometric flow ratios defined in the present work for Eqs. (1) and (2) are chosen at the fixed reference current density of 1 A cm^{-2}. Therefore the flow rates of fuel and oxidant are constant.

2.1. Assumptions

This model assumes:

- Two-dimensional.
- Steady-state flow.
- Ideal gas mixtures.
- Laminar and incompressible flow with low Reynolds numbers and pressure gradients.
- Negligible ohmic drop in the electronically conductive solid matrix of porous electrodes, and catalyst layers.
- Negligible Soret, Dufour, gravity and radiation effects.
- Isotropic and homogeneous electrodes, catalyst layers and membrane are characterized by effective porosities and permeabilities.
- Constant viscosity of gas mixture is calculated for the inlet condition.
- No contact resistance at the interfaces between different layers.

2.2. Governing equations

In contrast to the usual approach where separate differential equations are employed for different regions, here a unified single-domain approach with a single set of governing equations is applied to all regions. Based on the multi-domain method, the computational domain is divided into a number of sub-domains and different sets of conservation equations are developed for different sub-domains and the interfacial boundary conditions establish the connection between these equations. In the developed single-domain method, one set of conservation equations is considered for different regions of a PEM fuel cell. As a result, special numerical treatments have been used by defining extremely large or small physical and transport parameters in a region [1,11]. Therefore this model has a set of coupled non-linear partial differential equations including conservations of mass, momentum, species, energy and charge with electrochemical relations. The multiphase mixture model (M^2) is used for the two-phase flow that is an exact formulation of classical two-fluid, two-phase model having a single equation. The main difference between the M^2 model and the unsaturated flow theory is that the former does not require the approximation of constant gas-phase pressure. Another important feature of the M^2 model is that it can be easily used in a problem where single and double phase zones co-exist leading to a substantial decrease in the numerical complexity [1,24–29].

Mass conservation: Conservation of mass for the two-phase mixture using the M^2 model is as follows:

$$\nabla \cdot (\rho \vec{u}) = 0 \tag{3}$$

where $\vec{u}$ and ρ are mixture velocity and density, respectively [24,25].

$$\rho = \rho_l s + \rho_g (1 - s) \tag{4}$$

s and $(1 - s)$ are the fraction of open pore space occupied by the liquid and gas phases, respectively.

Momentum conservation: Conservation of momentum for the two-phase mixture with mixture velocity $\vec{u}$ can be written as:

$$\frac{1}{\varepsilon^2} \nabla \cdot (\rho \vec{u} \vec{u}) = -\nabla p + \nabla \cdot (\mu \nabla \vec{u}) + S_{Dar} \tag{5}$$

where μ is mixture viscosity defined as [24]:

$$\mu = \rho \left[\frac{k_{rl}}{\nu_l} + \frac{k_{rg}}{\nu_g} \right]^{-1} \tag{6}$$

In porous regions, superficial velocities are used in order to automatically ensure mass flux continuity at the interfaces between porous and non-porous regions. Also intrinsic transport properties in the porous regions are changed into effective transport properties taking into account the effects of porosity and tortuosity using Bruggeman correlation [1]. The source term of momentum equations in Table 1 is employed to consider Darcys law under the limiting condition where the permeability of porous media is small, resulting in low velocity.

Species conservation: Conservation of species equation using the M^2 model, in terms of molar concentration is as follows [26]:

$$\nabla(\gamma_C^i \vec{u} C^i) = \nabla[D_g^{i,eff} \nabla C_g^i] - \nabla \left[\left(\frac{mf_l^i}{M^i} - \frac{C_g^i}{\rho_g} \right) \vec{j}_l \right] + S_k \tag{7}$$

where C^i is the total concentration of species i in the liquid and gas phases. The liquid and gas phases have different flow-fields so the advective transport of species is corrected using the following correction factor, γ_c [1]:

$$\gamma_C = \begin{cases} \dfrac{\rho}{C^{H_2O}} \left(\dfrac{\lambda_l}{M^{H_2O}} + \lambda_g \dfrac{C_{sat}^{H_2O}}{\rho_g} \right) & \text{for water} \\ \dfrac{\rho \lambda_g}{\rho_g (1 - s)} & \text{for other species} \end{cases} \tag{8}$$

where λ_l and λ_g are the relative mobility of liquid and gas phases, respectively [24].

$$\lambda_k = \frac{k_{rk}/\nu_k}{\sum_k k_{rk}/\nu_k} \tag{9}$$

ν_k is the kinematic viscosity, k denotes the liquid or gas phase, k_{rl} and k_{rg} are the relative permeabilities of liquid and gas phases, respectively [15].

$$k_{rg} = (1 - s)^3, \quad k_{rl} = s^3 \tag{10}$$

The ρmf^i is mass fraction of species i, in terms of s:

$$\rho mf^i = \rho_g mf_g^i (1 - s) + \rho_l mf_l^i s \tag{11}$$

The second term on the right-hand side of the species conservation equation represents the capillary transport using the theory of capillary transport in hydrophobic GDL developed by Pasaogullari

Table 1
Source terms for momentum, species, energy and charge conservation equations for various regions.

Equation	Source terms			
	Flow channels	GDLs	Catalyst layers	Membrane
Momentum	$S_{Dar} = 0$	$S_{Dar} = -\frac{\mu}{K}\vec{u}$	$S_{Dar} = -\frac{\mu}{K}\vec{u}$	$S_{Dar} = -\frac{\mu}{K}\vec{u}$
Species	$S_k = 0$	$S_k = 0$	$S_k = -\nabla \cdot \left(\frac{n_d}{F} I \right) - \frac{s_k j}{nF}$	$S_k = -\nabla \cdot \left(\frac{n_d}{F} I \right)$
Energy	$S_T = h_{fg} \dot{m}_{fg}$	$S_T = h_{fg} \dot{m}_{fg}$	$S_T = j \left(\eta + T \frac{dU_0}{dT} \right) + \frac{I^2}{\kappa^{eff}} + h_{fg} \dot{m}_{fg}$	$S_T = \frac{I^2}{\kappa^{eff}} + h_{fg} \dot{m}_{fg}$
Charge	$S_e = 0$	$S_e = 0$	$S_e = j$	$S_e = 0$

Electrochemical reaction: $\sum s_k M_k = ne^-$ where $\begin{cases} M_k: & \text{chemical formula of species k} \\ s_k: & \text{stoichiometry coefficient} \\ n: & \text{number of electrons transferred} \end{cases}$,

anode hydrogen oxidation reaction (HOR) $H_2 - 2H^+ \rightarrow 2e^-$, cathode oxygen reduction reaction (ORR) $2H_2O - O_2 - 4H^+ \rightarrow 4e^-$.

Table 2
Physical and transport properties.

Parameter	Value
Water vapor activity	$a = \dfrac{c_g^{H_2O} RT}{P_{sat}} = \dfrac{c^{H_2O}}{c_{sat}^{H_2O}}$
Ionic conductivity of membrane ($S\,m^{-1}$)	$\kappa = (0.5139\lambda - 0.326)\exp\left(1268.0\left(\frac{1}{303} - \frac{1}{T}\right)\right)$
Polymer water content	$\lambda = \begin{cases} 0.043 + 17.81a - 39.85a^2 + 36.0a^3 & 0 < a \le 1 \\ 14 + 1.4(a-1) & 1 < a \le 3 \\ 16.8 & a > 3 \end{cases}$
Electro-osmotic drag coefficient	$n_d = \begin{cases} 1.0 & \lambda \le 14 \\ \dfrac{1.5}{8}(\lambda - 14) + 1.0 & \text{otherwise} \end{cases}$
Water diffusivity in membrane ($m^2\,s^{-1}$)	$D_e^{H_2O} = \begin{cases} 3.1 \times 10^{-7}\lambda(e^{0.28\lambda} - 1)\,e^{(-2346/T)} & 0 < \lambda \le 3 \\ 4.17 \times 10^{-8}\lambda(1 + 161e^{-\lambda})\,e^{(-2346/T)} & \lambda > 3 \end{cases}$
Gas diffusivity ($m^2\,s^{-1}$)	$D_g = D_0\left(\frac{T}{T_0}\right)^{1.5}\left(\frac{P}{P_0}\right)$
Gas density ($kg\,m^{-3}$)	$\rho_g = \dfrac{P}{RT\sum(w_i/M_i)}$

and Wang [1]. In the absence of gravity, liquid flux, $\vec{j}_l$ is given by [24,26]:

$$\vec{j}_l = \frac{\lambda_l \lambda_g}{\nu} K \nabla p_c \qquad (12)$$

p_c is the capillary pressure defined as [25]:

$$p_c = \sigma\,\cos(\theta_c)\left(\frac{\varepsilon}{K}\right)^{1/2} J(s) \qquad (13)$$

where $J(s)$, Leverett function is given for both the hydrophobic and hydrophilic GDL layers [30].

$$J(s) = \begin{cases} 1.417(1-s) - 2.120(1-s)^2 + 1.263(1-s)^3, & \text{if } \theta_c < 90^\circ \\ 1.417s - 2.120s^2 + 1.263s^3 & \text{if } \theta_c > 90^\circ \end{cases} \qquad (14)$$

The gas phase diffusion coefficient is modified to be effective using Bruggeman correlation [18] to account for the effects of porosity and tortuosity of the porous electrodes and catalyst layers. Also in the two-phase zones where the gas phase could be saturated with water vapor, the equation is modified by the liquid saturation. Note that in an isothermal model the water vapor concentration in the two-phase zone takes the saturation value, thus the molecular diffusion of water vapor disappear ($D_g^{i,\text{eff}} = 0$) [1]. In the non-isothermal situation, the water vapor saturation concentration that is a strong function of temperature, varies and therefore the vapor phase diffusion emerges as a new transport mechanism in the two-phase zone [18].

$$D_g^{i,\text{eff}} = [\varepsilon(1-s)]^{1.5} D_g^i \qquad (15)$$

The sources terms of species conservation equations in Table 1, are the representative of source or sink terms due to the electro-osmotic drag of water in the membrane and electrochemical reactions in catalyst layers.

Electronic charge conservation: Conservation of electronic charge equation is:

$$\nabla \cdot (\kappa^{\text{eff}} \nabla \phi_e) + S_e = 0 \qquad (16)$$

This equation describes proton transport inside the membrane–electrode assembly. The dependence of proton conductivity on water content is calculated using the empirical expression of Springer et al. [31,8] as shown in Table 2. The effective proton conductivity in porous media is described using the Bruggeman relation [8].

$$\kappa^{\text{eff}} = \varepsilon^{1.5}\kappa \qquad (17)$$

The source term for the charge equation in Table 1 represents the transfer of current between the electronically conductive solid matrix and the electrolyte for both the anode and cathode catalyst layers. In a PEM fuel cell, the anode hydrogen oxidation reaction exhibits fast electrokinetics with a low surface overpotential; therefore, it can easily be expressed by a linear equation, whereas the cathode oxygen reduction reaction has a relatively slow kinetics with a higher surface overpotential, which is adequately described by Tafel kinetics and is summarized in Table 3.

Energy conservation: Conservation of energy equation using the M^2 model is as follow [18]:

$$\nabla.(\gamma_h \rho c_p \vec{u} T) = \nabla.(k^{\text{eff}} \nabla T) + S_T \qquad (18)$$

The heat terms in the above-mentioned equation, as shown in Table 1, contain irreversible heat of the electrochemical reaction, reversible entropic heat, Joule heating, and an extra source due to condensation and evaporation. In the last source term, h_{fg} is the latent heat of condensation or evaporation and $\dot{m}_{fg}$ is the mass flow rate due to phase change that can readily be calculated from the continuity equation of the liquid phase [18,32]:

$$\dot{m}_{fg} = \nabla \cdot (\rho_l \vec{u}_l) = \nabla \cdot (\vec{j}_l + \lambda_l \rho \vec{u}) \qquad (19)$$

Since the pore size and advection in the GDL are relatively small, the temperature in solid and fluid phases are assumed to be equal. The advective term in Eq. (18) due to different flow fields of liquid and gas phases is corrected using the following correction factor,
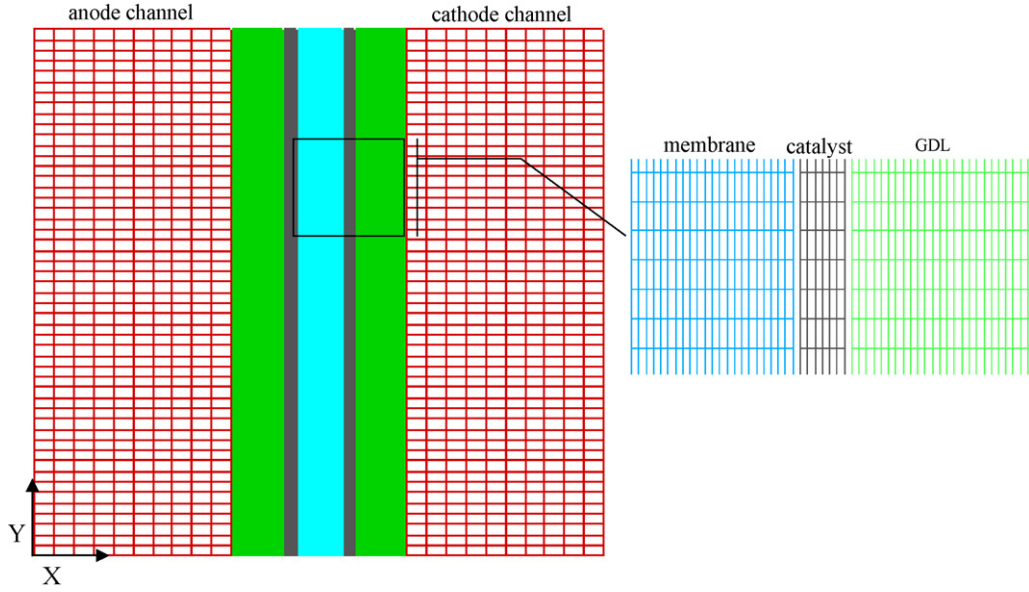
Table 3
Electrochemical properties.

Parameter	Anode	Cathode
Transfer current density ($A\,m^{-3}$)	$j = ai_{0,a}\left(\frac{c_{H_2}}{c_{H_2}^{\text{ref}}}\right)^{1/2}\left(\frac{\alpha_a + \alpha_c}{RT}F\eta\right)$	$j = -ai_{0,c}\left(\frac{c_{O_2}}{c_{O_2}^{\text{ref}}}\right)\exp\left(-\frac{\alpha_c}{RT}F\eta\right)$
Surface overpotential (V)	$\eta = \phi_s - \phi_e - U_o\,(\phi_s = 0)$	$\eta = \phi_s - \phi_e - U_o\,(\phi_s = V_{\text{cell}})$
Open circuit potential (V)	$U_o = 0$	$U_o = 1.23 - 0.9 \times 10^{-3}\,(T - 298.15)$
Transfer coefficient	$\alpha_a + \alpha_c = 2$	$\alpha_c = 1$
Exchange current density times reaction surface area ($A\,m^{-3}$)	$ai_{0,e} = 10 \times 10^9$	$ai_{0,e}(353) = 2.0 \times 10^4$

$ai_{0,c}(T) = (1-s)ai_{0,c}(353)\exp\left(-16,456\left(\frac{1}{T} - \frac{1}{353}\right)\right).$

Fig. 1. Two-dimensional geometry and computational mesh for PEM fuel cell model.

γ_h [18]

$$\gamma_h = \frac{\rho(\lambda_l c_{p,l} + \lambda_g c_{p,g})}{s\rho_l c_{p,l} + (1-s)\rho_g c_{p,g}} \quad (20)$$

The physical and transport properties in the above mentioned equations are presented in Table 2.

2.3. Boundary conditions

The complete set of governing equations representing the mathematical model is given by Eqs. (3), (5), (7), (16) and (18) that forms a set of equations with seven unknowns: $\vec{u}$, p, C^{H_2}, C^{O_2}, C^{H_2O}, ϕ_e and T. The advantage of this model is that only the external boundary conditions are required in this single-domain formulation. The boundary conditions are specified as follows.

2.3.1. Inlet boundaries

The inlet velocity in the gas channels are expressed by the respective stoichiometric flow ratio:

$$\vec{u}_{a,in} \cdot \vec{u}_{a,in} = U_{a,in}; \quad \vec{u}_{c,in} \cdot \vec{u}_{c,in} = U_{c,in} \quad (21)$$

$U_{a,in}$ and $U_{c,in}$ are derived from Eqs. (1) and (2). The molar concentrations of species are determined by the inlet pressure and humidity according to the ideal gas law.

$$C_{a,in}^{H_2O} = x_{a,in}^{H_2O}\frac{P_{a,in}}{RT_{a,in}} = RH_{a,in}\frac{P_{sat}}{P_{a,in}}\frac{P_{a,in}}{RT_{a,in}}$$

$$C_{c,in}^{H_2O} = x_{c,in}^{H_2O}\frac{P_{c,in}}{RT_{c,in}} = RH_{c,in}\frac{P_{sat}}{P_{c,in}}\frac{P_{c,in}}{RT_{c,in}} \quad (22)$$

Since summation of mole fraction species at anode and cathode inlets are unit, also the ratio of nitrogen and oxygen in dry air is known to be 79:21, the inlet hydrogen and oxygen concentration can be found via:

$$C_{a,in}^{H_2} = (1 - x_{a,in}^{H_2O})\frac{P_{a,in}}{RT_{a,in}} = \left(1 - RH_{a,in}\frac{P_{sat}}{P_{a,in}}\right)\frac{P_{a,in}}{RT_{a,in}}$$

$$C_{c,in}^{O_2} = x_{c,in}^{O_2}\frac{P_{c,in}}{RT_{c,in}} = \frac{1 - x_{c,in}^{H_2O}}{1 + 79/21}\frac{P_{c,in}}{RT_{c,in}} \quad (23)$$

A constant temperature is applied to the anode and cathode gas inlets.

$$T_{a,in} = T_{cell}; \quad T_{c,in} = T_{cell} \quad (24)$$

2.3.2. Outlet boundaries

The flow at the outlet is assumed to be fully developed or no-flux with a given back pressure.

$$\frac{\partial \vec{u}}{\partial n} = 0; \quad \frac{\partial C^i}{\partial n} = 0; \quad \frac{\partial \phi_e}{\partial n} = 0; \quad \frac{\partial T}{\partial n} = 0 \quad (25)$$

2.3.3. Walls

No-slip and impermeable velocity condition and no-flux condition (except at the outer boundary of anode and cathode channels for thermal boundary conditions) are applied:

$$\vec{u} = 0; \quad \frac{\partial P}{\partial n} = 0; \quad \frac{\partial C^i}{\partial n} = 0; \quad \frac{\partial \phi_e}{\partial n} = 0; \quad \frac{\partial T}{\partial n} = 0 \quad (26)$$

At the outer boundary of anode and cathode channels, either constant temperature or constant heat flux boundary conditions can be imposed [33]. Here constant temperature boundary condition is used [18].

$$T_{channel\,wall} = T_{cell} \quad (27)$$

2.4. Numerical procedures

The geometry and grid structure is given in Fig. 1 with the specifications listed in Table 4. Although commercial CFD programs are favored and widely used, still in-house programming has its own advantages due to a better control of a detailed modeling. The governing equations were discretized using a finite-volume method and solved using a developed code written in Fortran software. In this code the pressure and velocity fields are treated using SIMPLE pressure correction algorithm for a single-domain model. It should be mentioned that in spite of the absence of some species particularly in certain regions of fuel cell, the species transport equation can still be applied throughout the entire computational domain [34].

Stringent numerical tests were carried out to ensure that the solution was independent of grid size. At least 250 computational volumes in the along channel and 50, 30, 10 and 60 computational

Table 4
Dimensional parameters and transport properties.

Description	Unit	Value
Dimensional parameters		
Cell length	mm	70
Channel thickness	mm	1
Gas diffusion layer thickness	μm	300
Catalyst thickness	μm	10
Membrane thickness	μm	50.8
Operating conditions		
Cell temperature	K	353.0
Anode/cathode pressure	atm	1.5
Anode/cathode stoichiometry, ζ	–	2.0
Anode dry gas mole fraction	–	0.0
Cathode dry gas mole fraction	–	3.76
Transport parameters		
Reference hydrogen molar concentration, $C_{H_2}^{ref}$	mol m^{-3}	40.88
Reference oxygen molar concentration, $C_{O_2}^{ref}$	mol m^{-3}	40.88
Faraday's constant, F	C mol^{-1}	96,487
Universal gas constant, R	J mol^{-1} K^{-1}	8.34
Anode gas viscosity	pa s	1.101×10^{-5}
Cathode gas viscosity	pa s	1.881×10^{-5}
Liquid water viscosity at 80 °C	pa s	3.56×10^{-4}
H_2 diffusivity in the anode gas channel	m^2 s^{-1}	5.457×10^{-5}
H_2O diffusivity in the anode gas channel	m^2 s^{-1}	5.457×10^{-5}
O_2 diffusivity in the cathode gas channel	m^2 s^{-1}	1.806×10^{-5}
H_2O diffusivity in the cathode gas channel	m^2 s^{-1}	2.236×10^{-5}
Anode/cathode GDL porosity, ε_{GDL}	–	0.6
Anode/cathode catalyst layer porosity, ε_{cat}	–	0.6
Volume fraction of membrane in catalyst layers, ε_{mc}	–	0.26
Anode/cathode GDL permeability, K_{GDL}	m^2	6.875×10^{-13}
Contact angle of GDL, θ_c	°	110
Surface tension, σ	N m^{-1}	0.0625
Equivalent weight of membrane, EW	kg mol^{-1}	1.1
Dry density of membrane, ρ_{dry}	kg m^{-3}	1.98×10^3
Thermal conductivity of hydrogen	W m^{-1} K^{-1}	0.2040
Thermal conductivity of oxygen	W m^{-1} K^{-1}	0.0296
Thermal conductivity of nitrogen	W m^{-1} K^{-1}	0.0293
Thermal conductivity of water vapor	W m^{-1} K^{-1}	0.0237
Thermal conductivity of liquid water	W m^{-1} K^{-1}	0.67
Thermal conductivity of membrane	W m^{-1} K^{-1}	0.950
Thermal conductivity of GDL	W m^{-1} K^{-1}	0.5

Fig. 2. Flowchart of the simulation process.

at high current densities, specially phase changes at low operating temperature are neglected.

3.2. Effect of temperature on phase change

In this section, a two-phase non-isothermal model is developed to simulate the two-phase phenomena in a single straight-channel of a PEM fuel cell. Special attention has been given to the impact of the interfacial liquid accumulation on GDL, temperature distribution, and interaction between phase change and heat transfer.

volumes along the thickness of each channel, GDL, catalyst layer and membrane, respectively, are used. For a two-dimensional flow field, this grid requirement results in approximately 60,000 computational cells. The coupled set of equations was solved iteratively, and the solution was checked to be convergent when the relative error in each field between two consecutive iterations was less than 10^{-6}. The flowchart for this simulation is shown in Fig. 2. The CPU time range is between 5 and 6 h on a Pentium IV PC (3.2 GHz, 1 GB RAM).

3. Results and discussion

3.1. Model validation

For validation purpose, the data of a fuel cell operated under no humidity and low operating temperature (50 °C) is considered [35]. The simulation is carried out using the developed model for the same experimental conditions. The derived polarization curve is compared with both the experimental data presented by Buchi and Srinivasan and the single-phase model presented by Um and Wang [10] (see Fig. 3). The obtained results from this model show very good agreement with the measured experimental data with a deviation of less than 7% which could be as a result of 2D modeling where the rib effects are not considered. At high current densities, the results are in better agreement with the experimental data compared with Um and Wang results. This is due to the fact that their model is a single phase one where the effects of phase changes
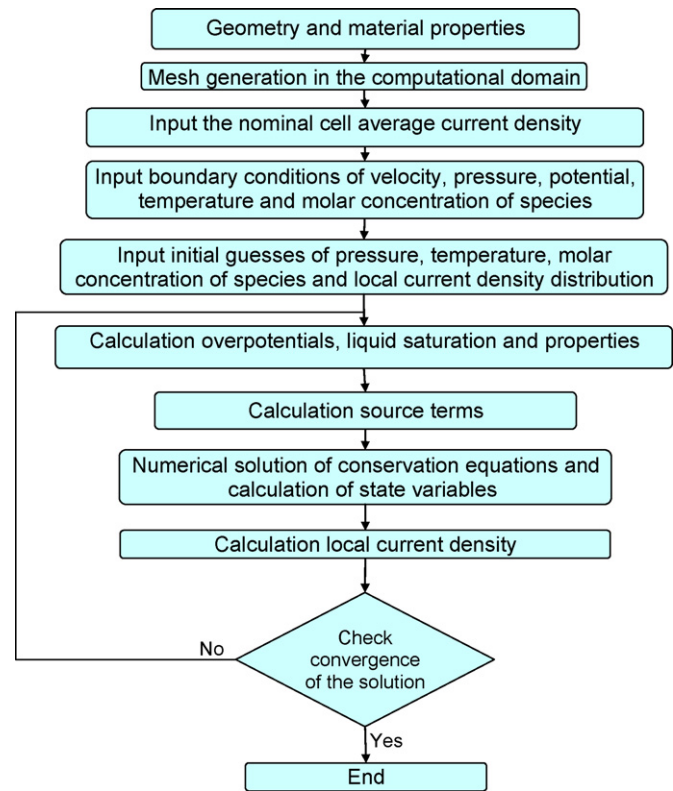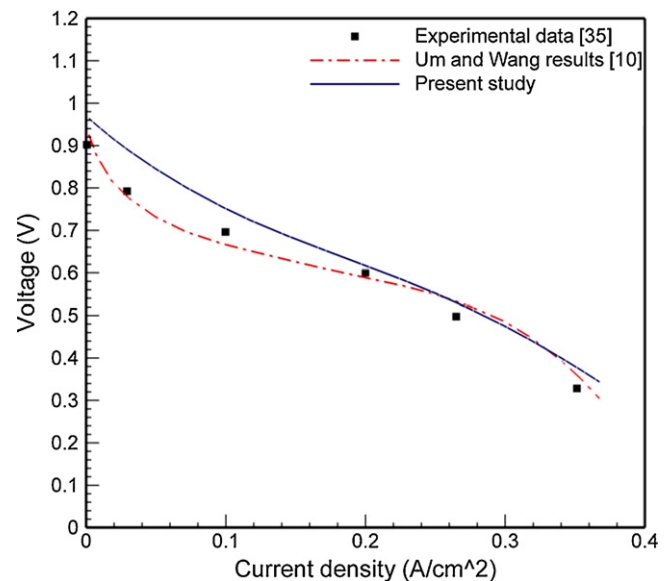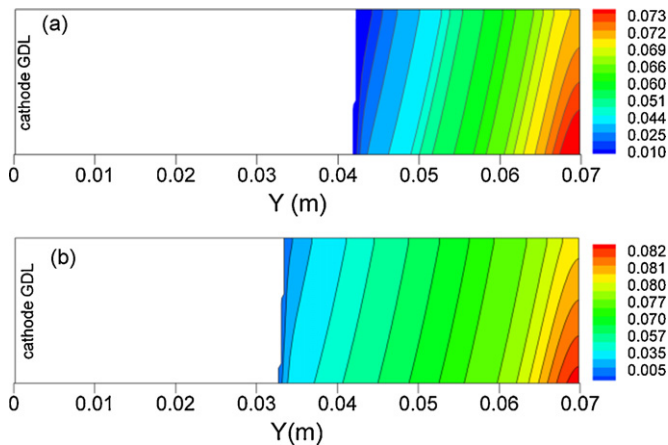

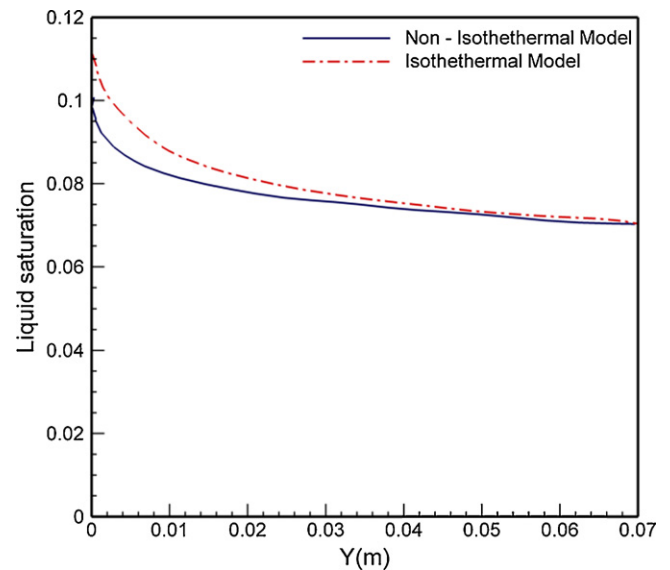**Fig. 3.** Comparison presented study with an experimental polarization curve and a single-phase model.

Fig. 4. (a) Liquid saturation distribution at cathode GDL for non-isothermal model at $V_{cell} = 0.55$ V for AFCL case (b). Liquid saturation distribution at cathode GDL for isothermal model at $V_{cell} = 0.55$ V for AFCL case.
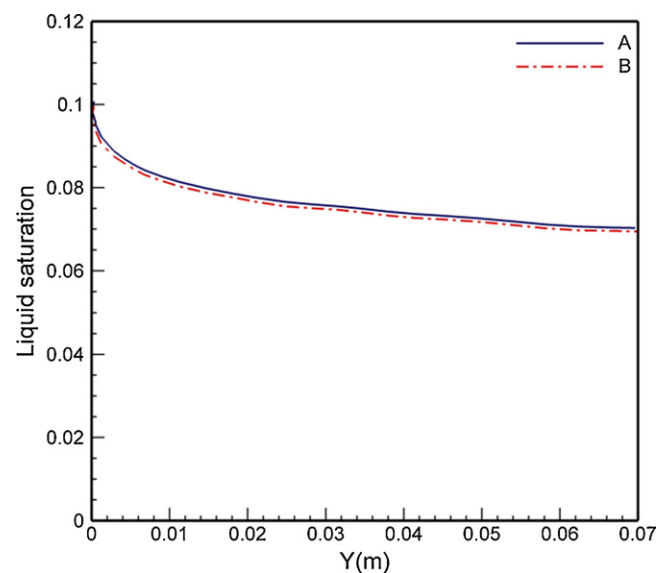

Fig. 5. Liquid saturation profiles at cathode GDL/catalyst layer interface along the channel direction for non- and isothermal models at $V_{cell} = 0.55$ V for AFCF case.

A two-dimensional simulation is performed when both anode and cathode inlet gas streams are fully humidified (AFCF) and when the anode inlet flow is fully humidified with low cathode flow humidification (AFCL). An inlet stoichiometric ratio of 2 is chosen for both anode and cathode sides based on a reference current density of 1 A cm^{-2}, therefore the flow rates are fixed for anode and cathode. The temperature and pressure are 80 °C and 1.5 atm at the inlets of both anode and cathode and the physicochemical and transport properties are listed in Table 4.

The numerically predicted liquid saturation distribution at GDL cathode side at 0.55 V is shown in Fig. 4a and b for AFCL case, for both the isothermal and non-isothermal models. At this voltage, the water may condense, but this does not occur until the water vapor concentration in the gas reaches the saturation level. The condensation with its location directly related to the local temperature and condensation front is then pushed downstream. In the non-isothermal model, up to a certain point along its lengths ($y = 0.045$ m), the GDL is free of any liquid water after which the stream of liquid water starts to appear. In the isothermal model, the water condensation and accumulation occur further upstream towards the inlet of the channel at $y = 0.032$ m, where the amount of liquid saturation is higher in the isothermal compared with the non-isothermal model. This is because in non-isothermal model, the temperature within the distance between $y = 0.032$ and $y = L$ is about 1.8 °C higher than that of the isothermal model. The increase in temperature causes an increase in saturation concentration, so less water vapor changes phase.

The liquid saturation level for isothermal and non-isothermal models for the AFCF case at cathode GDL/catalyst layer interface is shown in Fig. 5. In both cases, the maximum liquid saturation occurs near the inlet and decreases in the flow direction due to decreasing water production in the channel length. The amount of liquid saturation along the channel in the isothermal model is more than the non-isothermal one, where the maximum deviation for both cases appears at the entrance where the cell temperature is highest. The maximum level of liquid saturation is 12% and 10% for isothermal and non-isothermal models, respectively. Further along the channel the temperature drop causes the deviation to decrease as well where the vapor saturation concentration is a strong function of temperature.

In a non-isothermal two-phase zone is water transport in vapor diffusion mode due to variation in saturation vapor concentration with temperature. This mode of vapor diffusion is from the high temperature to low temperature regions. For investigated of this mode of vapor-phase diffusion as driven by the temperature

gradient, the liquid saturation level for the AFCF case at cathode GDL/catalyst layer interface with and without considering effect of temperature gradient on vapor-phase diffusion is compared and presented in Fig. 6. When we consider effect of temperature gradient on vapor-phase diffusion, water transport from the higher temperature to the lower temperature regions (see Fig. 7). In this state, liquid saturation slightly higher, because of the vapor-phase diffusion that moves water vapor from the water vapor production in catalyst layer and the water that income from cathode channel to the cathode GDL for condensation.

3.3. Effect of phase change on cell temperature

The temperature contours for a PEM fuel cell at 0.55 V for AFCL case is shown in Fig. 7, where the temperature rise is due to the heat generation caused by the exothermic nature of reactions, entropic heat, Joule heating and the water phase change. The maximum

Fig. 6. Liquid saturation profiles at cathode GDL/catalyst layer interface along the channel direction, with (state A) and without (state B) considering vapor-phase diffusion by the temperature gradient, $V_{cell} = 0.55$ V for AFCF case.
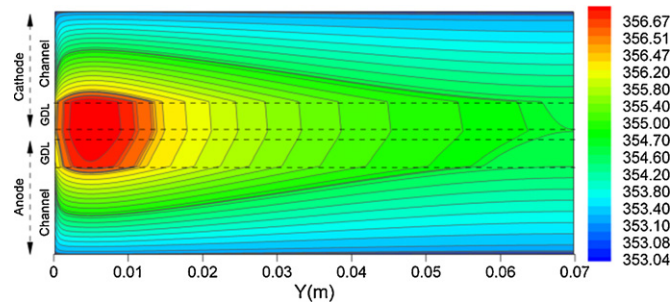
Fig. 7. Temperature distribution at $V_{cell} = 0.55$ V for AFCL case.

temperature occurs near the entrance because most of the heat is generated due to electrochemical reaction at the catalyst layer where the local current density is the highest at the inlet. The maximum temperature difference is observed to be 3.7 °C near the inlet and at the interface between membrane and catalyst layer in the cathode side where major heat generation takes place. Unlike channels, velocity in the membrane–electrode assembly is very low, therefore heat generation in the cell is carried downstream smaller by bulk motion and is primarily removed through the gas diffusion layer by conduction. This process could be controlled by the GDL thermal conductivity or feed gas relative humidity, as inlet humidification strongly affects the degree of overall membrane hydration.

The vapor-phase diffusion in the non-isothermal two-phase zone could cause to phase change heat transfer by water evaporation at the hotter regions and vapor condensation on the cooler regions of the cell. This mode of phase change heat transfer is conventionally referred to as the heat pipe effect. Fig. 8 shows comparison the temperature profiles along the channel direction at cathode GDL/catalyst layer interface, with and without considering phase change heat transfer due to vapor-phase diffusion. It can be seen that the first state has a slightly smaller temperature rise in the cell. The maximum temperature deviation between two states is about 0.1 K that appears near the inlet.

To have a better understanding of the effects phase change on temperature distribution, a detailed comparison between the single and two-phase models for AFCL and AFCF cases has been made. The temperature profiles across the cell are shown in Fig. 9 at three
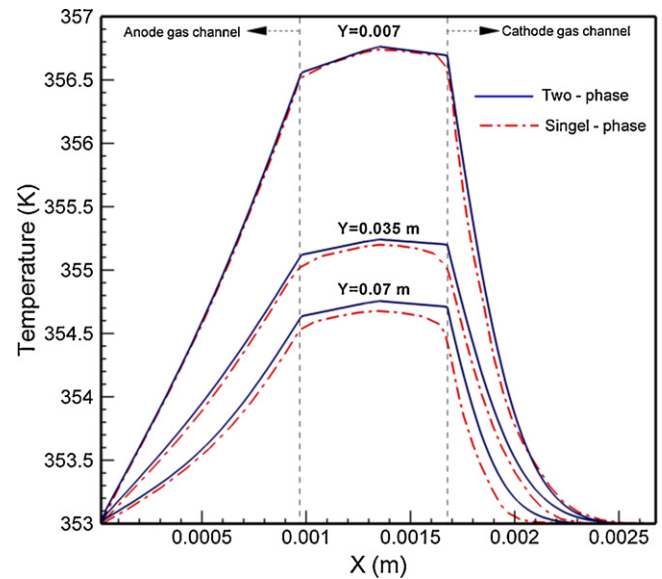

Fig. 9. Comparison temperatures profiles across cell direction at inlet, mid and outlet of channel at $V_{cell} = 0.55$ V between single- and two-phase models for AFCL case.

different sections, these are the inlet, middle and outlet zones for the AFCL case for the single and two-phase models. In the two-phase model, the phase change dose not occur at the beginning of the channel and the heat release due to phase change would have a smaller effect on the maximum temperature that appear in the cell inlet. The maximum difference occurs near the exits of both the cathode channel and the GDL for both the single and two-phase models, where phase change takes place and the heat generated by condensation would increase the temperature.

For the AFCF case, the cell temperature at all zones for two-phase model is higher due to the phase change that appear at the inlet as shown in Fig. 10. The maximum deviation in temperature for both models occurs near inlet at GDL cathode and cathode channel. The temperature distribution is seen to be in good agreement with the available data [32] where the minor difference could be due to single-phase assumption versus our two-phase model.
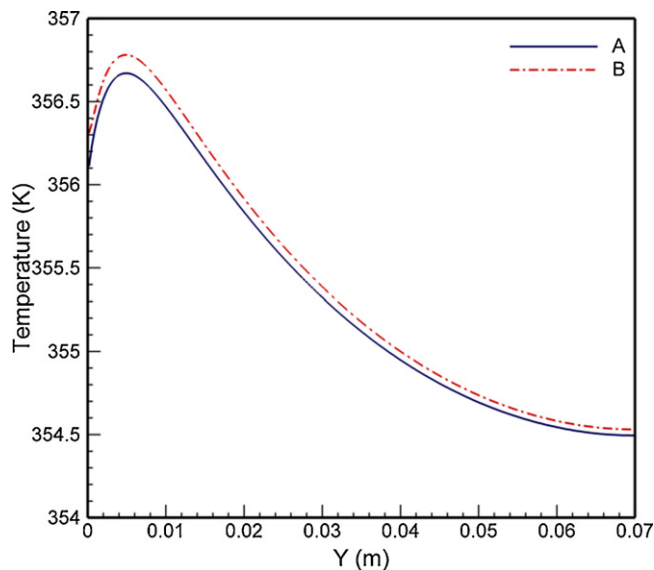

Fig. 8. Temperatures profile along the channel direction at cathode GDL/catalyst layer interface, with (state A) and without (state B) considering phase change heat transfer by vapor-phase diffusion, $V_{cell} = 0.55$ V for AFCF case.

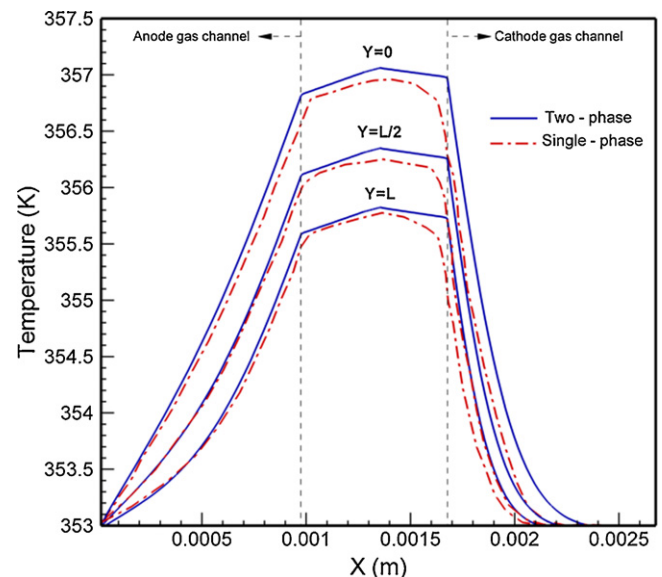**Fig. 10.** Comparison temperatures profiles across cell direction at inlet, mid and outlet of channel at $V_{cell} = 0.55$ V between single- and two-phase models for AFCF case.
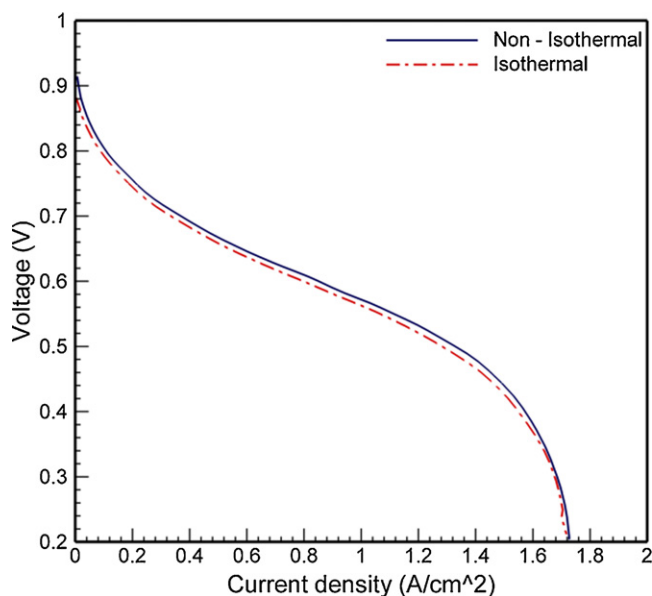
Fig. 11. Comparison of polarization curves from isothermal and non-isothermal calculations.

3.4. Comparison of isothermal and non-isothermal model predictions

A two-phase non-isothermal transport phenomena in PEM fuel cell operation is studied in detail and comparison between the isothermal and non-isothermal model predictions for the AFCL case, has been made. A complete steady state polarization curve predicted by the isothermal and non-isothermal models are shown in Fig. 11. At low current densities, the cell voltage prediction for the non-isothermal model is higher than that of the isothermal model. This is because in non-isothermal model, the cell temperature would increase the exchange current density as shown in Table 3. At higher current densities ($0.3 < I_{ave} < 1.2\,A\,cm^{-2}$), the cell voltage would be higher for the non-isothermal model, due to the fact that the increase in cell temperature would improve the cell potential owing to the reduced losses in the cell and increase in the ionic conductivity that leads to smaller resistive loss in the membrane. This can also reduce transport and activation losses. When the average current density is more than $1.2\,A\,cm^{-2}$, the cell operates at a limited mass transfer regime and there is a significant amount of water generated due to electrochemical reaction in the cathode, leading to liquid water formation and flooding of the cathode GDL. In the isothermal model, saturation concentration is smaller due to decreasing temperature, resulting in higher amounts of liquid water formation in the cathode GDL. Therefore, the cell performance is hampered in comparison with the non-isothermal model. However, high current densities could increase water vapor partial pressure, enhancing mass transport related losses.

4. Conclusions

A two-dimensional, two-phase, non-isothermal model where the conservation equations are coupled with electrochemical kinetics has been developed for a PEM fuel cell, based on a multi-phase mixture formulation to investigate the interaction between heat and water transport together with phase change. The main focus was to assess the results from coupling heat and transport phenomena in the fuel cell. The following conclusions are drawn:

- The temperature distribution is the most important parameter affecting the two-phase water transport, which controls the amount and location of liquid saturation.
- Partial humidification of the inlet air causes the liquid water to build up down stream at cathode GDL, whose generated location is temperature sensitive, so in the non-isothermal model, where temperature increase enhances saturation concentration, a larger portion along the channel length will be free of liquid water.
- Full humidification of the air at the inlet results in condensation and flooding at full face of GDL cathode, where the maximum liquid saturation at GDL cathode moves further up stream towards the inlet and decreases in the flow direction along the channel. The amount of liquid saturation in the isothermal model is more than the non-isothermal model, and the maximum deviation occurs at the entrance due to the extremely high temperature at the inlet.
- The PEM fuel cell temperature distribution is highly voltage sensitive; this model predicts the temperature differential to be about $3.7\,^{\circ}C$ at a chosen voltage of 0.55 V. The maximum temperature occurs near the inlet at the interface between the membrane and catalyst layer on the cathode side where major heat generation takes place.
- At partial humidification of inlet air, phase change would have a smaller effect on the maximum temperature that appears in the cell inlet, also the maximum temperature difference for single and two-phase models occur further down stream towards the exit of cathode channel and its GDL.
- At full humidification of the inlet air, the cell temperature at all regions for the two phase model is higher due to the phase change that occurs at the inlet, where the maximum temperature deviation for both models occurs further up stream in cathode channel and its GDL.
- Vapor-phase diffusion by providing a new mechanism for heat removal from the cell affects the temperature distribution. Instead, water transport via vapor-phase diffusion due to the temperature gradient.
- The accuracy of performance prediction by the non-isothermal model is better than the isothermal one, in which the temperature rise may increase the exchange current density and ionic conductivity or reduce flooding in the fuel cell.
- The present study successfully demonstrates the importance and accuracy of a coupled, two-phase heat and water transport model in a PEM fuel cell.

References

[1] U. Pasaogullari, C.Y. Wang, J. Electrochem. Soc. 152 (2005) A380–A390.
[2] I.S. Hussainia, C.Y. Wang, J. Power Sources 187 (2009) 444–451.
[3] J.J. Hwang, S.J. Liu, J. Power Sources 162 (2006) 1203–1212.
[4] H. Ju, C.Y. Wang, S. Cleghorn, U. Beuscherb, J. Electrochem. Soc. 153 (2006) A249–A254.
[5] T. Berning, N. Djilali, J. Power Sources 124 (2003) 440–452.
[6] J.J. Hwang, J. Electrochem. Soc. 153 (2) (2006) A216–A224.
[7] M.H. Akbari, B. Rismanchi, J. Renewable Energy 33 (2008) 1775–1783.
[8] H. Ju, H. Meng, C.Y. Wang, Int. J. Heat Mass Transfer 48 (2005) 1303–1315.
[9] F.Y. Zhang, X.G. Yang, C.Y. Wang, J. Electrochem. Soc. 153 (2006) A225–A232.
[10] S. Um, C.Y. Wang, J. Power Sources 156 (2006) 211–223.
[11] N.P. Siegel, M.W. Ellis, D.J. Nelson, M.R. Spakovsky, J. Power Sources 128 (2004) 173–184.
[12] L. You, H. Liu, J. Power Sources 155 (2006) 219–230.
[13] A. Rowe, X. Li, J. Power Sources 102 (2001) 82–96.
[14] V. Mishra, F. Yang, R. Pitchumani, J. Power Sources 141 (2005) 47–64.
[15] T. Berning, N. Djlali, J. Electrochem. Soc. 150 (2003) A1589–A1598.
[16] S. Mazumder, J.V. Cole, J. Electrochem. Soc. 150 (2003) A1510–A1517.
[17] E. Birgersson, M. Noponen, M. Vynnycky, J. Electrochem. Soc. 152 (2005) A1021–A1034.
[18] Y. Wang, C.Y. Wang, J. Electrochem. Soc. 153 (2006) A1193–1200.
[19] J.J. Hwang, J. Power Sources 164 (2007) 174–181.
[20] U. Pasaogullari, P.P. Mukherjee, C.Y. Wang, K.S. Chen, J. Electrochem. Soc. 154 (2007) B823–B834.
[21] J. Yuan, B. Sunden, J. Electrochim. Acta 50 (2004) 677–683.
[22] E. Afshari, S.A. Jazayeri, Am. J. Appl. Sci. 6 (2009) 101–108.

[23] E. Afshari, S.A. Jazayeri, Proceedings of ASME European Fuel Cell Technology & Applications EFC2007, Rome, Italy, December 11–14, 2007.
[24] C.Y. Wang, P. Cheng, J. Adv. Heat Transfer 30 (1997) 93–196.
[25] C.Y. Wang, P. Cheng, Int. J. Heat Mass Transfer 39 (1996) 3607–3618.
[26] U. Pasaogullari, C.Y. Wang, Electrochim. Acta 49 (2004) 4359–4369.
[27] H. Meng, C.Y. Wang, J. Electrochem. Soc. 151 (3) (2004) A358–A367.
[28] Z.H. Wang, C.Y. Wang, K.S. Chen, J. Power Sources 94 (1) (2001) 40–50.
[29] Y. Wang, C.Y. Wang, J. Power Sources 153 (2006) 130–135.
[30] U. Pasaogullari, C.Y. Wang, J. Electrochem. Soc. 151 (3) (2004) A399–406.
[31] T.E. Springer, T.A. Zawodinski, S. Gottesfeld, J. Electrochem. Soc. 136 (1991) 2334–2341.
[32] C.Y. Wang, Chem. Rev. 104 (2004) 4727–4766.
[33] S. Um, Ph.D. thesis, Pennsylvania State University, University Park, 2003.
[34] S.V. Patankar, Numerical Heat Transfer and Fluid Flow, Hemisphere, PA, New York, 1980.
[35] F.N. Buchi, S. Srinivasan, J. Electrochem. Soc. 144 (1997) 2767–2773.